Sea-ice melt driven by ice-ocean stresses on the mesoscale

Mukund Gupta[1], **John Marshall**[1], **Hajoon Song**[2], **Jean-Michel Campin**[1], **Gianluca Meneghello**[1]

[1]Massachusetts Institute of Technology
[2]Yonsei University

Key Points:

- Ice-ocean drag on the mesoscale generates Ekman pumping that brings warm waters up to the surface
- This melts sea-ice in winter and spring and reduces its mean thickness by 10 % under compact ice regions
- Sea-ice formation (melt) in cyclones (anticyclones) produces deeper (shallower) mixed layer depths.

Corresponding author: Mukund Gupta, `guptam@mit.edu`

Abstract

The seasonal ice zone around both the Arctic and the Antarctic coasts is typically characterized by warm and salty waters underlying a cold and fresh layer that insulates sea-ice floating at the surface from vertical heat fluxes. Here we explore how a mesoscale eddy field rubbing against ice at the surface can, through Ekman-induced vertical motion, bring warm waters up to the surface and partially melt the ice. We dub this the 'Eddy Ice Pumping' mechanism (EIP). When sea-ice is relatively motionless, underlying mesoscale eddies experience a surface drag that generates Ekman upwelling in anticyclones and downwelling in cyclones. An eddy composite analysis of a Southern Ocean eddying channel model, capturing the interaction of the mesoscale with sea-ice, shows that within the compact ice zone, the mixed layer depth in cyclones is very deep ($\sim$ 500 m) due to brine rejection, and very shallow in anticyclones ($\sim$ 20 m) due to sea-ice melt. This asymmetry causes 'EIP' to warm the core of anticyclones without significantly affecting the temperature of cyclones, producing a net upward vertical heat flux that reduces the mean sea-ice thickness in the region by 10 % over the course of winter and spring. In the following months, the sea-ice thickness recovers with an overshoot, due to strong negative feedbacks associated with atmospheric cooling and salt stratification. Consequently, the 'EIP' mechanism does not accumulate over the years, but modulates the seasonal cycle of ice within the compact ice zone.

Plain Language Summary

Polar oceans typically have cold water at the surface and warmer waters at depth. When the atmospheric temperature is cold enough, the top layer of the ocean cools to the freezing point, and sea-ice forms at the surface. This growth can be impeded by warmer waters at depth, whose heat can melt sea-ice at its base. The effectiveness of this melting depends on the amount of heat transported from the deeper layers of the ocean up to the surface underneath the ice. This study explores a novel mechanism by which frictional interactions between ocean and sea-ice can increase the amount of heat delivered to the surface. At small scales (30 - 100 km), when the ocean rubs against relatively stationary sea-ice, it experiences a torque that drives vertical motions in the water column. This brings warmer waters in contact with sea-ice, and can reduces its mean thickness by 10 % over the course of winter and spring. In the following months, the ice thickness recovers due to restoring processes, such that this mechanism does not lead to accumulated melt over the years, but changes the seasonality of sea-ice.

1 Introduction

The sea-ice zone surrounding both the Arctic and Antarctic coasts is vulnerable to melt from underlying warm waters residing at depth. In the Arctic, the cold halocline layer limits upward oceanic heat fluxes to about 1 to 3 Wm^{-2} in the high Arctic in winter (Carmack et al., 2015) and allows multiyear sea-ice to grow several meters thick (Maksym, 2019). In the Antarctic, however, the upper ocean is more weakly stratified, and consequently heat is readily ventilated to the surface. Typical winter ocean heat fluxes can reach 25 to 35 Wm^{-2} (Martinson & Iannuzzi, 1989), which limits the thickness of sea-ice to a mean of 70 to 90 cm (Worby et al., 2008). Ackley et al. (2015) measure vertical heat fluxes of about 8 Wm^{-2} under pack ice in the Bellingshausen Sea and 17 Wm^{-2} under fast ice in the Amundsen Sea, respectively, consistent with co-located sea-ice melt rates. With rising oceanic temperatures, the role of these vertical heat fluxes on sea-ice melt is likely to keep increasing, as it has in the Arctic over the last decades (Carmack et al. (2015), Polyakov et al. (2017)). Future changes in sea-ice coverage and seasonality may also have a global impact through their influence on deep and bottom water formation in the Arctic (Mauritzen and Häkkinen (1997)) and Antarctic (Ohshima et al. (2016)), respectively.

The coarse resolution of Global Climate Models (GCMs) limits their ability to faithfully reproduce some of the fine scale physical processes responsible for vertical heat fluxes underneath sea-ice. These mechanisms may include double-diffusive mixing (Padman (1995), Timmermans et al. (2008), Sirevaag and Fer (2012)), mesoscale eddy stirring (McKee et al. (2019)), convection driven by brine rejection (Martinson & Iannuzzi, 1989) or interactions with the bathymetry (Muench et al., 2001), turbulence generated by ice/ocean drag (Ackley et al., 2015), inertial/tidal oscillations (Geiger et al., 1998), and internal wave mixing (Timmermans & Marshall, 2020). Over the Western Antarctic peninsula, McKee et al. (2019) present evidence that mesoscale eddies are responsible for delivering warm upper circumpolar deep waters to the continental shelf, consistent with the observations of Moffat and Meredith (2018). In the Arctic marginal ice zone (MIZ), previous studies have highlighted the importance of ocean eddies in the processes of heat and mass exchanges that control the sea-ice distribution (Johannessen et al. (1987), Niebauer and Smith Jr. (1989)). Manucharyan and Thompson (2017) describe a process by which intense, but small-scale, horizontal density gradients in the MIZ can enhance vertical velocities at the submesoscale and upwell warm waters to the surface.

This study explores a related mechanism termed 'Eddy-Ice-Pumping' (EIP), by which frictional ice/ocean interactions at the mesoscale may intensify vertical velocities within eddies and drive upward heat fluxes underneath the ice. In regions where the ice concentration is large enough to resist motion driven by eddies, sea-ice exerts a net drag τ_i upon the ocean surface, which opposes the eddy velocity u. As illustrated in Figure 1, this mechanism generates surface divergence and Ekman upwelling in anticyclones, while driving surface convergence and Ekman downwelling in cyclones. Given the temperature inversion underneath the ice, one expects an advection of warm waters towards the ice in antiyclones (favoring ice melt), and away from the ice in cyclones (limiting melt). We investigate how this mechanism affects the vertical structure of eddies and the overall melting rates in regions of compact sea-ice.

The modulation of eddy vertical velocities by surface stresses has been discussed in the context of air-sea interactions in the open ocean (McGillicuddy et al. (2007), Gaube et al. (2015), Song et al. (2020)). The difference between surface winds and currents can drive both a monopole (Dewar & Flierl, 1987) and a dipole (Stern (1965), Niiler (1969)) response in vertical velocities within eddies. Gaube et al. (2015) also find that Ekman velocities induced by sea surface temperature (SST) gradients can be significant in western boundary currents and in the Antarctic Circumpolar Current (ACC). Depending on their persistence, these vertical motions can significantly influence the life-cycle, structure and transport properties of eddies (McGillicuddy, 2016). Here, we examine the effectiveness of EIP at generating an eddy-scale curl in surface stress, and discuss whether the induced vertical velocities are persistent and large enough to affect the local profiles of temperature and salinity. We are also interested in how EIP couples with melting and freezing processes occurring in the seasonal ice zone.

The paper is structured as follows: Section 2 describes the Southern Ocean eddying channel model used to investigate the EIP mechanism. Section 3, explores the conditions under which this process occurs in the model. Section 4 presents an eddy composite analysis that highlights differences between the open ocean and the compact ice zone, the asymmetric response of cyclones and anticyclones to EIP, and the resulting modulation of sea-ice melt and formation. Section 5 describes the aggregate effects of EIP over a seasonal cycle and over multiple years in the compact ice zone. Section 6 discusses the main findings of this study and concludes.

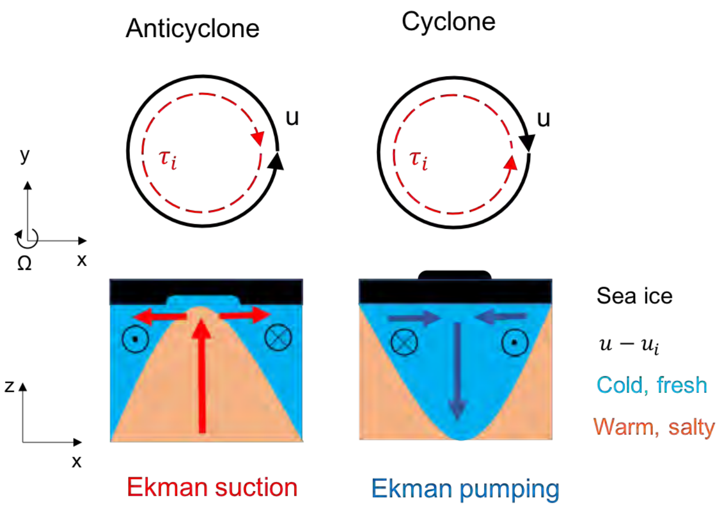

Figure 1. Schematic of the 'Eddy-Ice-Pumping' mechanism (EIP) in the Southern hemisphere. When sea-ice is stationary relative to the eddy, the ice-ocean stress τ_i opposes the eddy motion u, driving Ekman suction in anticyclones and Ekman pumping in cyclones. Upwelling of warm waters may melt sea-ice in anticyclones, whereas downwelling in cyclones may shield sea-ice away from warm waters, potentially allowing for thicker ice growth.

2 The 3D channel model

Numerical experiments are conducted using an eddying ocean-ice channel model based on the MIT general circulation model (MITgcm) (Marshall et al. (1997b), Marshall et al. (1997a), Adcroft et al. (1997)) representing the Southern Ocean and its seasonal ice zone. The domain has dimensions of 1200 km by 3200 km in the zonal and meridional directions respectively, with 4.08 km horizontal resolution. The east and west boundaries are connected, such that when fluid leaves from one side, it re-enters from the other. There are 50 vertical levels from the surface to the flat ocean bottom at 4000 m. The vertical resolution ranges from 10 m in the top 50 m up to 100 m near the bottom. At the Southern boundary, there is a 300 m deep and 80 km wide shelf, followed by a 220 km wide continental slope that drops to the bottom. This setup was introduced in Doddridge et al. (2019).

The model is initialized using temperature and salinity profiles from the World Ocean Atlas version 2 (Locarnini et al. (2013), Zweng et al. (2013)) along 30°E, and repeated in the zonal direction. The northern boundary has a 100 km wide sponge layer over which temperature and salinity are relaxed to the initial conditions on a 10 day timescale. At the surface, the channel is forced through bulk formulae (Large & Pond, 1982) by monthly mean atmospheric fields from the Corrected Normal Year Forcing Version 2.0 taken along 30°E (Large & Yeager, 2009). As with the initial conditions, the atmospheric fields are extended across the channel, such that there is no zonal variation in surface forcing. Vertical mixing is based on the turbulent kinetic energy scheme by Gaspar et al. (1990).

The sea-ice model is based on the formulation detailed in Losch et al. (2010). It uses a continuum representation of sea-ice properties such as concentration, thickness and velocity. Sea-ice thermodynamics employs the 3-layer model of Winton (2000), where ice and snow thicknesses are calculated using heat fluxes from the top and bottom surfaces. Sea-ice dynamics are based on the elastic-viscous-plastic formulation by Hunke and Dukowicz (1997) in which atmospheric, oceanic and internal stresses drive the sea-ice motion. The ice/ocean stress $\vec{\tau_i}$ is parameterized as follows:

$$\vec{\tau_i} = \rho_0 C_d (\vec{u} - \vec{u_i}) |\vec{u} - \vec{u_i}|, \tag{1}$$

where ρ_0 is the ocean density, C_d is a drag coefficient, $\vec{u}$ is the horizontal surface ocean velocity and $\vec{u_i}$ is the sea-ice velocity. The turning angle is assumed to be zero and the drag coefficient is kept to a constant value of $C_d = 5.17\ 10^{-3}$, consistent with the work of Mazloff et al. (2010) in the context of the Southern Ocean State Estimate (SOSE).

At the start of the simulation, the sea-ice thickness is initialized to 1 m, covering the entire model domain south of 56°S. The model is integrated for 50 years, by which time it reaches a quasi-equilibrium. Figure 2 shows the zonal and annual mean state of the model at equilibrium. The potential temperature distribution in the top panel highlights a temperature inversion between y = 400 - 1600 km, where cold and fresh waters in the top 10 - 100 m of the water column lie above warm and salty waters of northern origin. The residual meridional circulation consists of two overturning cells that upwell to surface around y = 800 km, bringing relatively warm waters in close proximity to the seasonal ice zone. In the top 50 - 100 m underneath the ice, isopycnals are relatively flat, due to the salinity stratification. Throughout this paper, the mixed layer depth (MLD) is defined as the depth at which the local difference in potential density with respect to the overlaying surface value is: $\Delta\sigma_0 = 0.06\ kgm^{-3}$. Our results are not particularly sensitive to the choice of this threshold in the range $\Delta\sigma_0 = 0.01$ - $0.1\ kgm^{-3}$. The MLD is relatively shallow (10 - 80 m) in the annual mean and in summer over the whole domain. Between y = 0 - 600 km, the winter MLD depth can extend down to 800 m, due to bottom water formation.

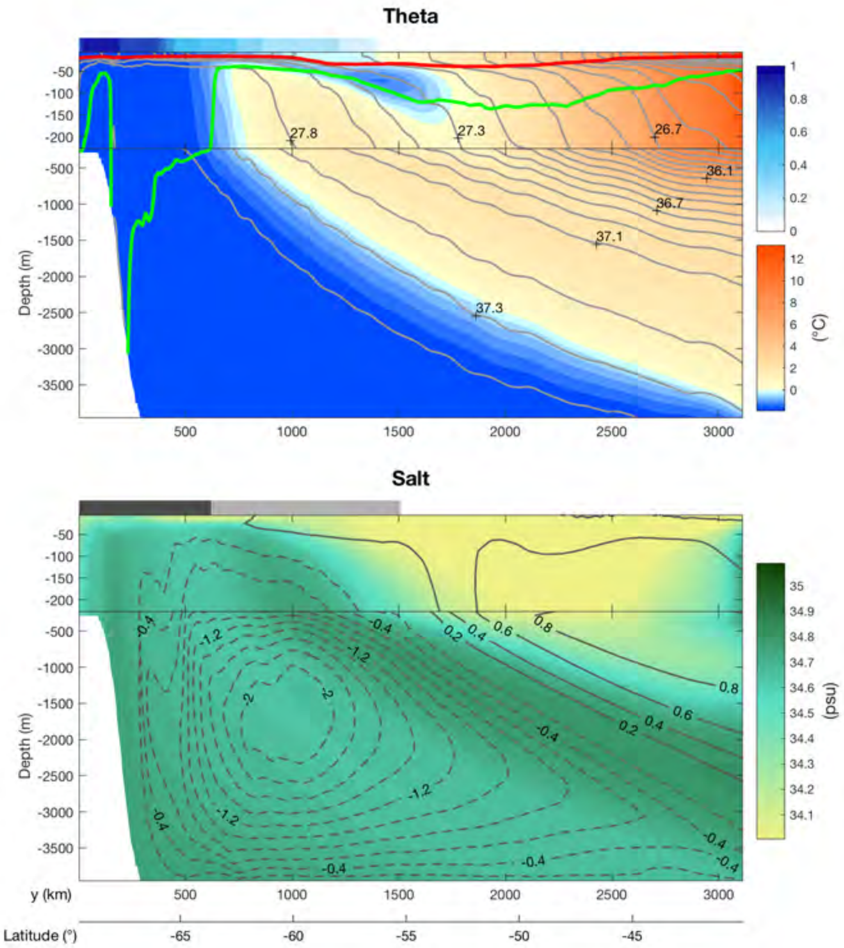

Figure 2. Annual and zonal mean state of the channel model at equilibrium. (Top) Potential temperature (filled contours), potential density σ_0 (grey line contours in the top 210 m) and σ_2 (grey contours between 210 - 4000 m). The annual mean sea-ice fraction is shown in the blue bars at the top of the panel. The colored lines show the summer (red) and winter (green) MLD, both based on a $\Delta\sigma_0 = 0.06\ kgm^{-3}$ criterion. (Bottom) Salt (filled contours) and residual streamfunction in Sv [$= 10^6 m^3 s^{-1}$] (grey line contours; filled clockwise, and dashed anticlockwise). The solid bars at the top of the panel indicate the minimum (dark grey) and maximum (light grey) sea-ice extent.

3 Exploration of 'Eddy-Ice-Pumping' in an idealized model

Figure 3 shows EIP at play from a snapshot of the channel model's ice zone taken in September. During that month, sea-ice cover is at its maximum extent, and a region of compact sea-ice develops in the southern part of the channel (panel (a)). The Rossby number (ζ/f, in panel (b)) reaches peak values of 0.5, and there is evidence of both cyclonic and anticyclonic mesoscale eddies present under the ice. The horizontal length-scale of these eddies ranges from tens to hundreds of kilometers and increases from south to north, due to the influences of the beta effect and the continental slope on the first baroclinic Rossby radius of deformation ($R_d = NH/f$). Using representative values of $N = 10^{-3}s^{-1}$, $f = 10^{-4}s^{-1}$ and $H = 250$ - 4000 m gives an R_d of 40 km off the shelf and 2.5 km on the shelf. Eddies on the shelf and parts of the continental slope therefore tend to be weaker than in the rest of the domain. The model's horizontal resolution of 4.08 km can resolve some of the mesoscale eddy features but perhaps not the finest scales. The band-like structure seen between y = 0 - 400 km in ζ/f and other quantities in Figure 3 is the result of using a wind forcing that is uniform in the zonal direction.

Panel (c) shows the vertical Ekman velocity w_{ek} computed as:

$$w_{ek} = \frac{1}{\rho_0} \nabla \times \left(\frac{\vec{\tau}}{f} \right), \tag{2}$$

where the net ocean stress $\vec{\tau}$ is a linear combination of the ice-ocean stress $\vec{\tau_i}$ and the wind-ocean stress $\vec{\tau_w}$, weighted by the sea-ice fraction α as follows:

$$\vec{\tau} = \alpha \vec{\tau_i} + (1 - \alpha) \vec{\tau_w}. \tag{3}$$

Between y = 0 - 800 km, where the sea-ice fraction is high ($\geq 80\%$), there is a small scale pattern of w_{ek} with magnitudes reaching up to 10 m/day. In this region, the pattern in w_{ek} is reflected on the subsurface vertical velocity w_s diagnosed at the first model layer (5 m depth) and shown in panel (d). In regions of loose ice (y = 800 - 1400 km), the difference between the sea-ice and ocean vorticities (ζ and ζ_i, shown in panel (e)) is negligibly small, reflecting a regime where sea-ice drift is strongly influenced by underlying ocean currents. On the other hand, when ice is compact, ζ and ζ_i are largely decoupled, due to internal stresses restricting the ice motion. The transfer of energy between ocean and sea-ice P_i can be computed as follows:

$$P_i = \vec{\tau_i} \cdot \vec{u}, \tag{4}$$

Panel (f) shows the eddying component of P_i, defined as:

$$P_i' = \vec{\tau_i'} \cdot \vec{u'}, \tag{5}$$

where the prime quantities are anomalies from the zonal mean. In regions of compact sea-ice, where the underlying eddy field is strong (y = 200 - 800 km), P_i' is significantly more negative than in the rest of the ice zone, and its spatial pattern matches that of w_{ek}. This is evidence of the ice exerting drag upon the ocean at the mesoscale, and inducing EIP.

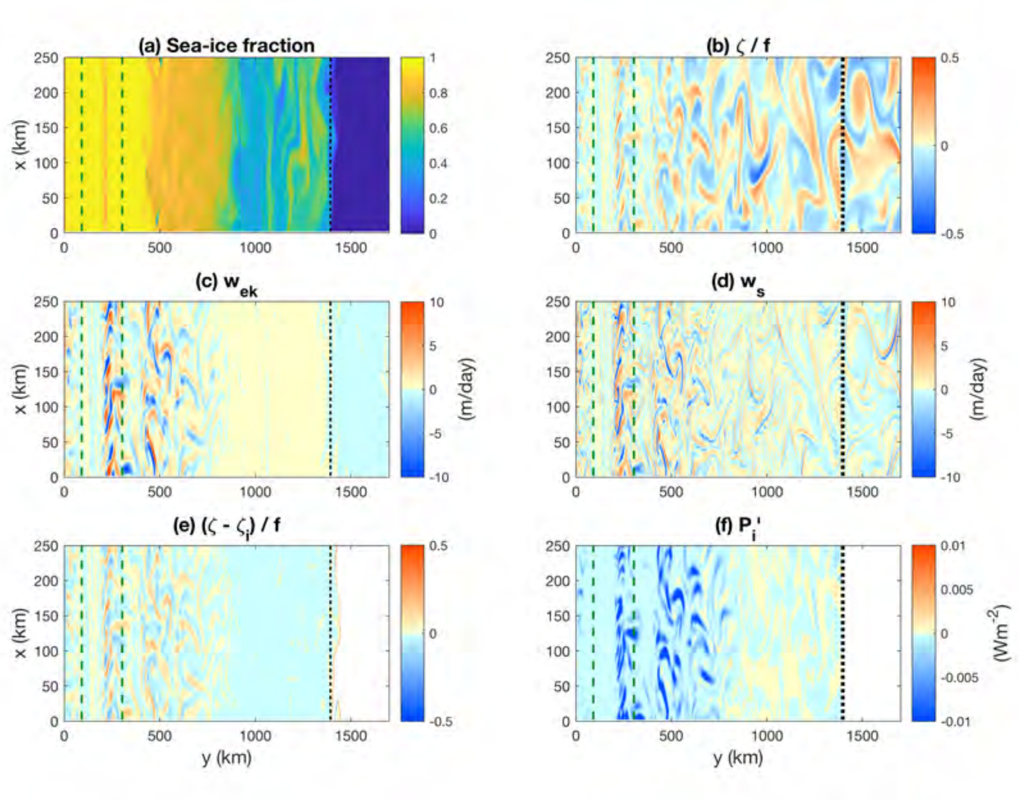

Figure 3. Snapshots taken in September and shown over a subset of the model domain for (a) sea-ice fraction, (b) normalized surface vorticity ζ/f (c) Ekman vertical velocity w_{ek}, (d) subsurface vertical velocity w_s, (e) normalized surface vorticity minus sea-ice vorticity (ζ - ζ_i)/f, and (f) eddying power transfer between ice and ocean P_i'. The green dashed lines show the limits of the continental slope and the shelf, and the dotted black line shows the zonal mean sea-ice edge.

The relatively large Rossby number of the flow ($\zeta/f \sim 0.3$) indicates that internal dynamics and wind-ocean interactions can generate significantly large vertical velocities within eddies, beyond the linear Ekman effect (Stern (1965), McGillicuddy et al. (2007), Thomas et al. (2008), Gaube et al. (2015)). This explains the filament-like structure in the diagnosed vertical velocity field (Figure 3 (d)) evident almost everywhere, including in regions of loose sea-ice and in the open ocean.

To separate the contribution of EIP from other factors enhancing vertical velocities, we design a simulation named ice stress 'off', in which the MITgcm code is modified such that the net stress felt by the ocean $\vec{\tau}$ ignores the ice-ocean stress $\vec{\tau_i}$ in Eq. (3). Instead, $\vec{\tau}$ is simply set to the open-ocean wind stress $\vec{\tau_w}$, which is much more zonally symmetric. The calculation of the net stress felt by sea-ice is left unchanged. To enable comparison with the control simulation (ice stress 'on'), we also decrease the input magnitude of the wind speeds in the ice zone, such that the zonal mean net stresses are comparable in the ice stress 'on' and 'off' simulations (see Figure 4). The scaled wind velocities $\vec{u_w^{sc}}$ were calculated from the original wind velocities $\vec{u_w}$ as follows:

$$\vec{u_w^{sc}} = (1 - \overline{\alpha}^C)\vec{u_w}, \tag{6}$$

where $\overline{\alpha}$ is the zonal mean sea-ice fraction. The exponent factor C was tuned offline to obtain a good match in the zonal mean stresses between the 'on' and 'off' simulations. We found that a value of C = 10 gives a reasonable agreement, both in the x and y directions (see Figure 4 (a-b)). That C is large implies that the zonal-mean stress is only significantly affected by sea-ice in regions of compact ice (high α), where the wind stress momentum is partially absorbed by sea-ice as internal stresses. When sea-ice is loose (low α), the wind transfers momentum to the ice, which in turn transfers it to the ocean without significant absorption. Figure 4 (c-d) shows how turning the ice stress 'off' reduces the scale and magnitude of the subsurface vertical velocities in the ice zone. In what follows, we investigate the differences between the ice stress 'on' and 'off' simulations, both at the eddy scale (Section 4) and when averaging over the compact ice zone (Section 5).

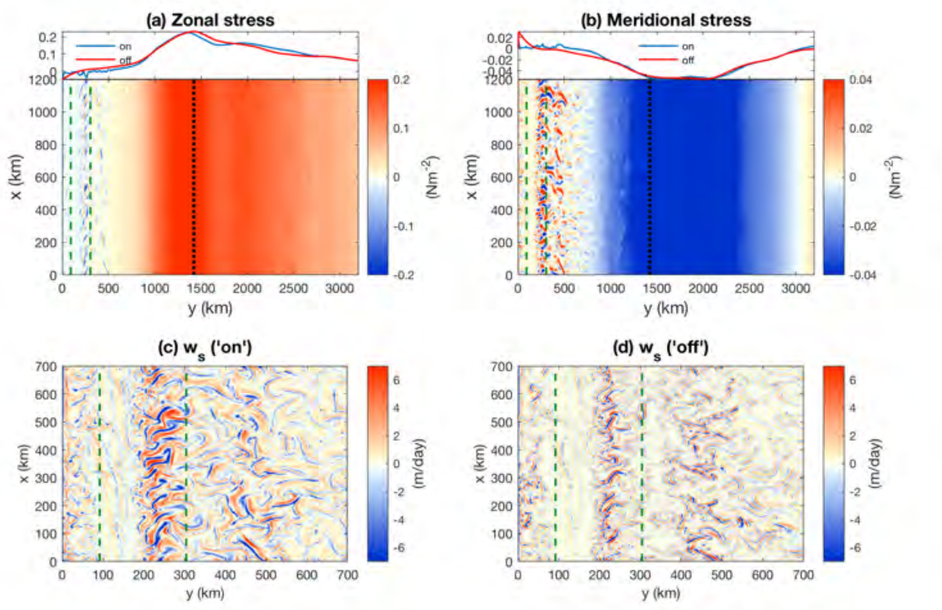

Figure 4. (a-b) September snapshots of (a) the zonal and (b) the meridional stresses on the ocean surface across the whole model domain. The colored contours show the net surface stresses in the simulation where the ice stress is 'on'. The line plots show zonal mean stresses for the simulations where the ice stress is 'on' (blue) and 'off' (red). (c-d) September snapshots of subsurface vertical velocity w_s within the ice zone for the cases where the ice stress is (c) 'on' and (d) 'off'. Note the different horizontal and vertical axes between (a-b) and (c-d). The green dashed lines indicate the edges of the continental slope and shelf respectively. The black dotted line shows the zonal mean sea-ice edge.

4 Eddy detection and compositing

In this section, we study the effects of EIP on eddies by compositing fields over cyclones and anticyclones, respectively, and averaging in the eddy-centric coordinate. Following Chelton et al. (2011), eddies are identified from closed sea surface height (SSH) anomalies and a set of criteria constraining their size and shape (as outlined in Appendix A). We detect eddies from 30 snapshots of SSH taken at 1-day interval during the month of September. The eddy size r is defined as the radius of the circle that encloses the SSH contour along which the surface current velocity is maximum (Chelton et al., 2011). The eddy-centric fields are horizontally interpolated onto a high-resolution grid spanning $-2r$ to $+2r$ in both the x and y directions. In the Southern Hemisphere, anticyclones (positive SSH) rotate counterclockwise, whereas cyclones (negative SSH) rotate clockwise. We perform the eddy composite analysis for three different cases, namely (i) the open ocean (Figure 5), (ii) the compact ice zone with ice stress 'on' (Figure 6), and (iii) the compact ice zone with ice stress 'off' (Figure 7).

4.1 Open Ocean

In the open ocean, composites are taken between y = 1900 - 2900 km, which is a region that is stratified in both temperature and salinity (see Figure 5). The composites are obtained by averaging over snapshots of 192 cyclones and 184 anticyclones, with mean sizes of 61 km for cyclones and 65 km for anticyclones, and mean sea surface heights of -14 cm for cyclones and 11 cm for anticyclones. The eddy characteristics found in this analysis are qualitatively consistent with the ones presented in past studies of Southern Ocean composites (Song et al. (2015), Hausmann et al. (2017)).

Open ocean cyclones are characterized by a cold and fresh anomaly at their core. The isopycnals bow upwards, and the MLD conforms to that curvature, shallowing at the core of the eddy. The vertical velocity shows enhanced downwelling at the western edge of the eddy, and upwelling at its eastern edge. Appendix B shows that the vertical velocity induced by eddy-wind interactions only modestly contributes to the diagnosed w_s, and that their patterns are not in phase. Instead, the zonal dipole in w_s is consistent with advection by eddies along background isopycnals that slope upward towards the south (see Figure 2). Poleward flow on the east of cyclones leads to upwelling, whereas equatorward flow on the west leads to downwelling.

Open ocean anticyclones display a mirrored structure from the cyclones. They have a warm and salty core, their isopycnals bow down, the MLD deepens, and the sign of the dipole in vertical velocity reverses. The diagnosed structure in w_s is again consistent with advection along the background isopycnal slope, generating downwelling on the eastern side of anticyclones and upwelling on their western side.

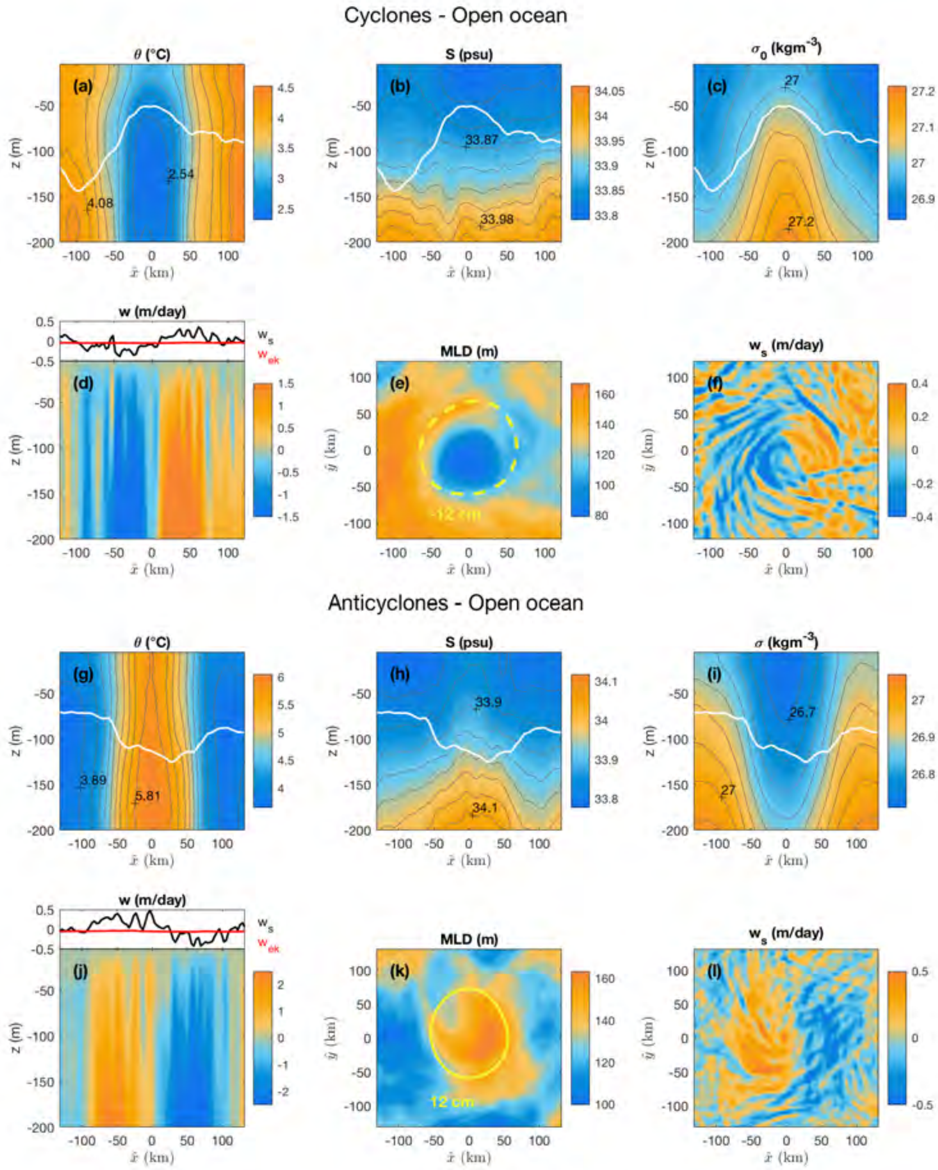

Figure 5. Open ocean composites taken between y = 1900 - 2900 km in the channel model for cyclones (panels (a) to (f)) and anticyclones (panels (g) to (l)). The composites are projected on to a characteristic eddy radius $\hat{r}$ = 60 km and the horizontal coordinates $\hat{x}$ and $\hat{y}$ span -2$\hat{r}$ to +2$\hat{r}$. The filled contours in panels (a) to (d) show vertical cross-sections through the center of the composite in the x-direction for θ, S, σ_0 and the vertical velocity w, respectively. The white lines in panels (a) to (c) indicate the MLD. Panel (d) also shows w_s (in black) and w_{ek} (in red). The filled contours in panels (e) and (f) show plan views of the MLD and w_s, respectively. The yellow line in panel (e) is a characteristic sea surface height contour. Panels (g) to (l) show corresponding results for the anticyclone composite.

4.2 Compact sea-ice - ice stress 'on'

Figure 6 shows eddy composites taken in the compact ice zone in the simulation where the ice stress is 'on'. The sampling domain is restricted to y = 400 - 800 km, since beyond y < 400 km, the entire water column is near the freezing temperature in September, which means that the Ekman-induced vertical velocities cannot significantly affect the melting of sea-ice. For y > 800 km, the sea-ice is too loose for EIP to play a significant role, as discussed in Section 3. In the region y = 400 - 800 km, the top 100 m of the water column is characterised by a temperature inversion (cold over warm) and salinity stratification (see Figure 2). The rest of the column is only weakly stratified. The composites are obtained by averaging over snapshots of 231 cyclones and 174 anticyclones, with mean sizes of 31 km for cyclones and 32 km for anticyclones, and mean sea surface heights of -4 cm for cyclones and 4 cm for anticyclones.

As in the open ocean, cyclones within the compact ice show a negative temperature anomaly at their core. Near the surface, the temperature is at the freezing point, which drives sea-ice formation. Within the composite cyclone, the sea-ice is 0.2 m thicker than the mean (1 m), and the net heat flux to the ice is about -15 Wm^{-2} (freezing). In the top 30 m, brine rejection associated with sea-ice formation causes a salty cyclone core. Between 30 - 200 m, the core is relatively fresh, as was seen in the open ocean. The edges of the cyclone still show the zonal dipole in vertical velocity that was evident in the open ocean (downward motion in the west and upward motion in the east). The isopycnals bow up everywhere, but unlike in the open ocean, the MLD is very deep at the center of the cyclone ($\sim$ 500 m). This is likely caused by the strong downwelling velocity at the core of the eddy evident in the vertical velocity profile. Panel (d) shows that w_{ek} (red line) can only partially explain the diagnosed subsurface velocity w_s (black line). We thus argue that the central downwelling is driven by both EIP and brine rejection.

In anticyclones, the situation is mostly reversed from cyclones, but with some important distinctions. As in the open ocean, there is a warm temperature anomaly at the eddy core, which here tends to melt sea-ice and produce a fresh core in the top 30 m. Within the anticyclone, the ice is 0.2 m thinner than the mean (1 m), and the net heat flux to the ice is approximately +15 Wm^{-2} (melting). Between 30 - 200 m, the core is saltier than the edges, as was seen in the open ocean. The edges of the anticyclone still show the zonal dipole in vertical velocity that was evident in the open ocean (upward motion in the west and downward motion in the east). The isopycnals bow down everywhere, but unlike in the open ocean, the MLD is anomalously shallow at the core, due to increased stratification from sea-ice melt. The warm and salty properties of the eddy are enhanced by upwelling at the core bringing deeper waters up to the surface. We argue that this upward motion is favored by EIP, as evidenced by the good match between w_s (black line) and w_{ek} (red line) shown in panel (d).

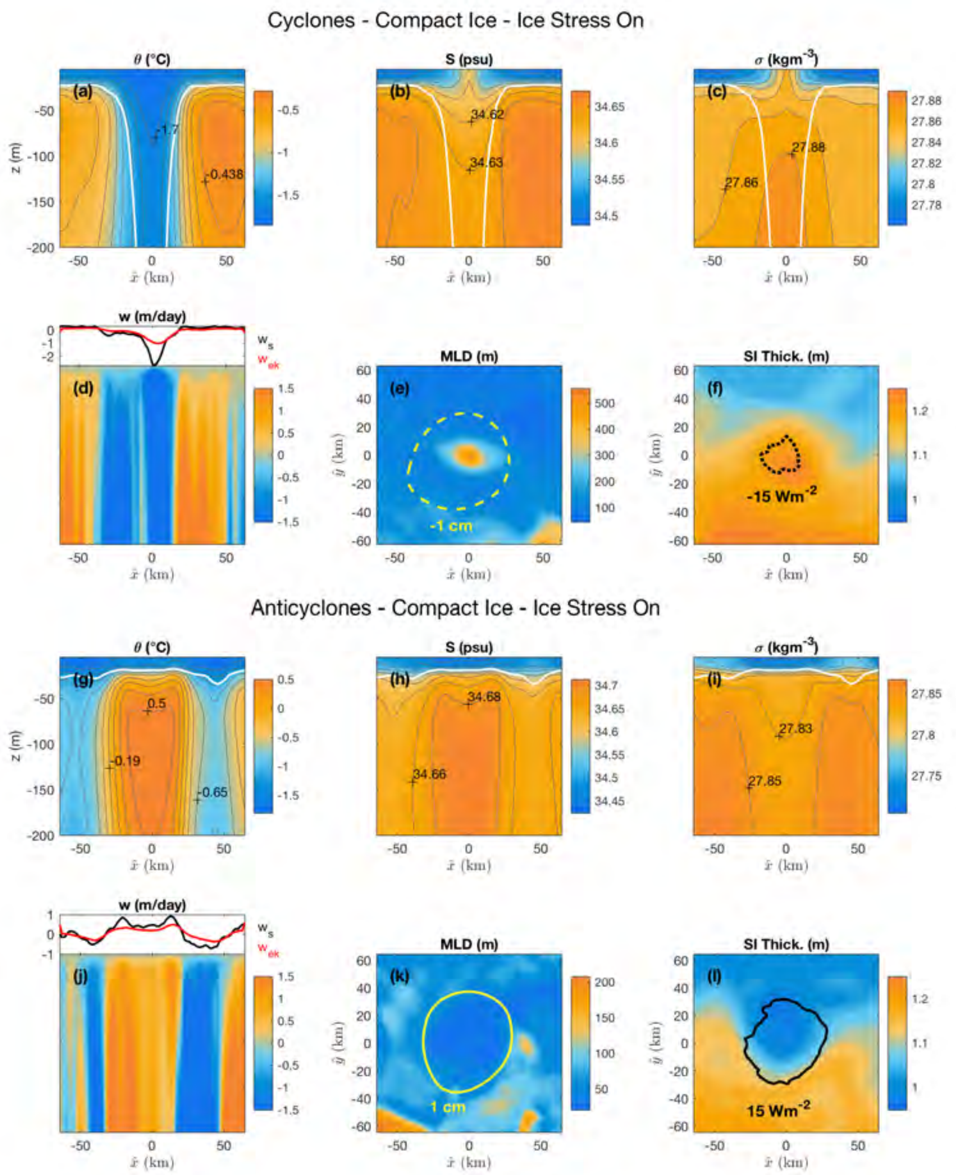

Figure 6. Compact ice zone composites with ice stress 'on' taken between y = 400 - 800 km in the channel model for cyclones (panels (a) to (f)) and anticyclones (panels (g) to (l)). The composites are projected on to a characteristic eddy radius $\hat{r}$ = 30 km and the horizontal coordinates $\hat{x}$ and $\hat{y}$ span -2$\hat{r}$ to +2$\hat{r}$. The filled contours in panels (a) to (d) show vertical cross-sections through the center of the composite in the x-direction for θ, S, σ_0 and the vertical velocity w, respectively. The white lines in panels (a) to (c) indicate the MLD. Panel (d) also shows w_s (in black) and w_{ek} (in red). The filled contours in panels (e) and (f) show plan views of the MLD and the area-weighted average sea-ice thickness, respectively. The yellow line in panel (e) is a characteristic sea surface height contour. The black line in panel (f) is the net heat flux to the ice. Panels (g) to (l) show corresponding results for the anticyclone composite.

4.3 Compact sea-ice - ice stress 'off'

To assess the effect of EIP on the eddy structure, we again take composites in the compact ice zone between y = 400 - 800 km, but in the simulation where the ice stress is 'off' (see Figure 7). The composite mean is obtained by averaging over snapshots of 259 cyclones and 218 anticyclones, with mean sizes of 31 km for cyclones and 32 km for anticyclones, and mean sea surface heights of -4 cm for cyclones and 4 cm for anticyclones.

The composited cyclone profiles are similar between the ice stress 'on' and 'off' cases. The temperature is near freezing at the surface and the cyclone is still a site of sea-ice formation, as evidenced by thicker sea-ice at the eddy core and a net flux to the ice that is comparable to the 'on' case (-15 Wm^{-2}). The eddy edge is again characterized by a zonal dipole in vertical velocity, as in the open ocean. However, in this case, the Ekman pumping velocity is zero (red line in panel (d)), and the diagnosed surface downwelling velocity at the core (black line in panel (d)) is lower than in the ice stress 'on' case (1 m/day instead of 2 m/day). The remaining downward velocity at the core is still relatively strong, and likely driven by brine rejection. Consequently, the MLD remains very deep ($\sim$ 500 m).

In anticyclones, the composite profiles are also similar between the ice stress 'on' and 'off' simulations, but there are some notable differences. The Ekman suction velocity is zero (red line in panel (d)), and thus the diagnosed vertical velocity at the eddy core is weak. Instead, the vertical velocity profile looks similar to that found in the open ocean, with the zonal dipole at the eddy edges. The lack of upward motion at the eddy center limits the amount of warm waters brought up to the surface, which reduces the temperature of the eddy core by approximately 0.1°C relative to the 'on' case. The sea-ice thickness is only 0.1 m thinner than the mean, and the net heat flux acting to melt sea-ice is +7 Wm^{-2} (compared to 0.2 m and +15 Wm^{-2}, respectively, in the ice stress 'on' case). The MLD still shallows at the eddy core, but slightly less than when the ice stress is 'on', due to reduced sea-ice melt.

In summary, cyclones and anticyclones are sites of sea-ice formation and melt, respectively. In cyclones, brine rejection produces a deep MLD ($\sim$ 500 m), whereas in anticyclones sea-ice melt shallows the MLD ($\sim$ 20 m). EIP upwells warmer waters to the surface in anticyclones, enhancing sea-ice melt. In cyclones, the downwelling at the eddy core is caused by both EIP and brine rejection. Turning EIP 'off' reduces the downwelling, but does not change sea-ice formation, since the surface is still near the freezing temperature.

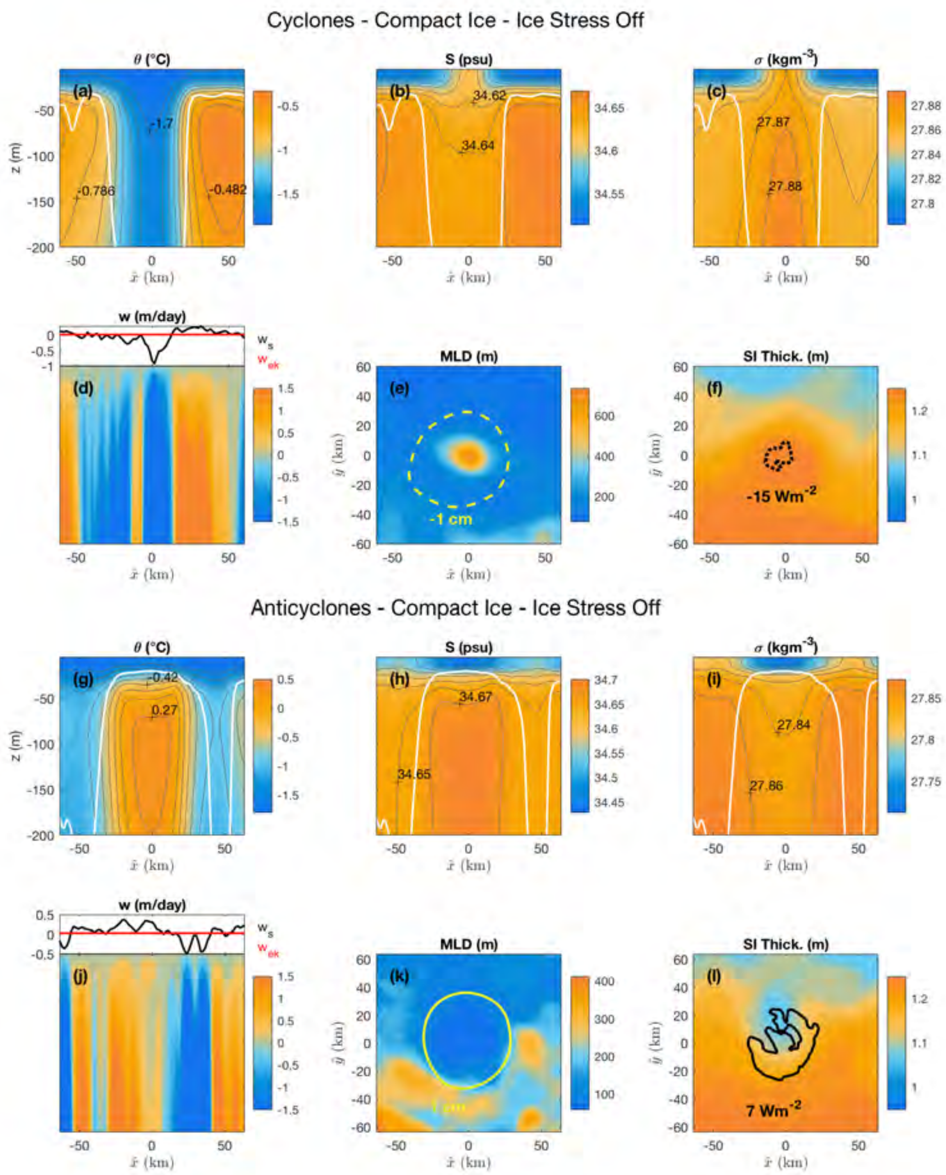

Figure 7. Compact ice zone composites with ice stress 'off' taken between y = 400 - 800 km in the channel model for cyclones (panels (a) to (f)) and anticyclones (panels (g) to (l)). The composites are projected on to a characteristic eddy radius $\hat{r}$ = 30 km and the horizontal coordinates $\hat{x}$ and $\hat{y}$ span -2$\hat{r}$ to +2$\hat{r}$. The filled contours in panels (a) to (d) show vertical cross-sections through the center of the composite in the x-direction for θ, S, σ_0 and the vertical velocity w, respectively. The white lines in panels (a) to (c) indicate the MLD. Panel (d) also shows w_s (in black) and w_{ek} (in red). The filled contours in panels (e) and (f) show plan views of the MLD and the area-weighted average sea-ice thickness, respectively. The yellow line in panel (e) is a characteristic sea surface height contour. The black line in panel (f) is the net heat flux to the ice. Panels (g) to (l) show corresponding results for the anticyclone composite.

5 Aggregate effects of eddy-ice interaction

In this section, we investigate whether the anomalous melt in anticyclones caused by EIP can have any significant aggregate effect on the system's mean state. Figure 8 shows the seasonal evolution of zonal mean heat fluxes and sea-ice thickness evaluated within the compact ice zone (y = 400 - 800 km) over one year of the simulation. We calculate the vertical heat flux H at the surface as:

$$H = \rho c_w w\theta, \tag{7}$$

and decompose H into its mean ($\overline{H} = \rho c_w \overline{w}\overline{\theta}$) and eddying ($H' = \rho c_w \overline{w'\theta'}$) components, where deviations are taken from the zonal mean. We also consider the net heat absorbed or provided by sea-ice from its surroundings for melt or formation, respectively.

In the control simulation (ice stress 'on'), Figure 8 shows that sea-ice formation occurs mostly between April and July, and sea-ice melt from September to March. The mean sea-ice thickness grows from 0 to 1.2 m between February and June, and stays approximately constant until November. The presence of the ice stress tends to increase the net vertical heat fluxes towards the ice, particularly between August and October (an increase of approximately 3 - 5 Wm^{-2}). The increase in H is mostly driven by the eddying component H', with the mean component $\overline{H}$ being significantly weaker. This enhanced upward heat flux is reflected in the melting rate, which increases by 2 - 4 Wm^{-2} during those months. Consequently, the mean sea-ice thickness decreases by 13 cm (about 10 %) over the course of winter and spring.

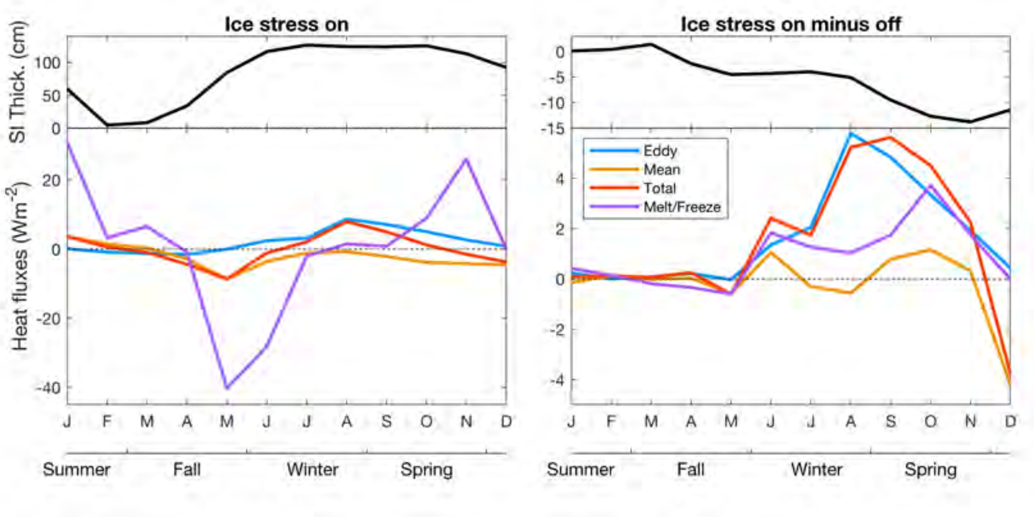

Figure 8. Seasonal evolution of the area-weighted average sea-ice thickness (top) and heat fluxes (bottom) within the compact ice zone (y = 400 - 800 km) calculated for the first year of the sensitivity simulation; (left) ice stress 'on', and (right) ice stress 'on' minus 'off'.

In Figure 9, we investigate the seasonal effect of EIP on mean vertical profiles within the compact ice zone (y = 400 - 800 km), by comparing the simulations with ice stress 'on' and 'off'. In the control simulation, θ remains around -1°C for the whole year below 40 m depth. In the top 40 m, the temperature varies seasonally up to 1°C in summer and down to freezing (-1.8°C) in winter and spring. The salinity below 40 m depth is 34.7 psu year-round, but varies seasonally between 34.7 psu (in winter and spring) and 33.5 psu (in summer and fall) in the top 40 m. The N^2 profile has a peak around 20 m depth that is strongest in summer and fall, weak in spring, and absent in winter. The EKE profiles have a peak around 20 - 50 m depth, but otherwise decrease monotonically with depth. Near the surface, EKE tends to be slightly larger in winter and spring compared to summer and fall.

The difference between the ice stress 'on' and 'off' simulations shows warming on the order of 0.15°C between 20 - 40 m depth during winter and spring, consistent with EIP bringing warm waters up closer to the surface during those months. The top 20 m is only marginally warmer, likely due to some of the upwelled heat transferred to the atmosphere and the ice. EIP only has a marked effect on salinity in spring, during which the top 30 m freshens by approximately 0.04 psu, driven by sea-ice melt. This near-surface warming and freshening increases the peak in stratification at 20 m depth. The dissipation of oceanic energy against sea-ice tends to decrease EKE throughout the water column in spring, but not during the other seasons.

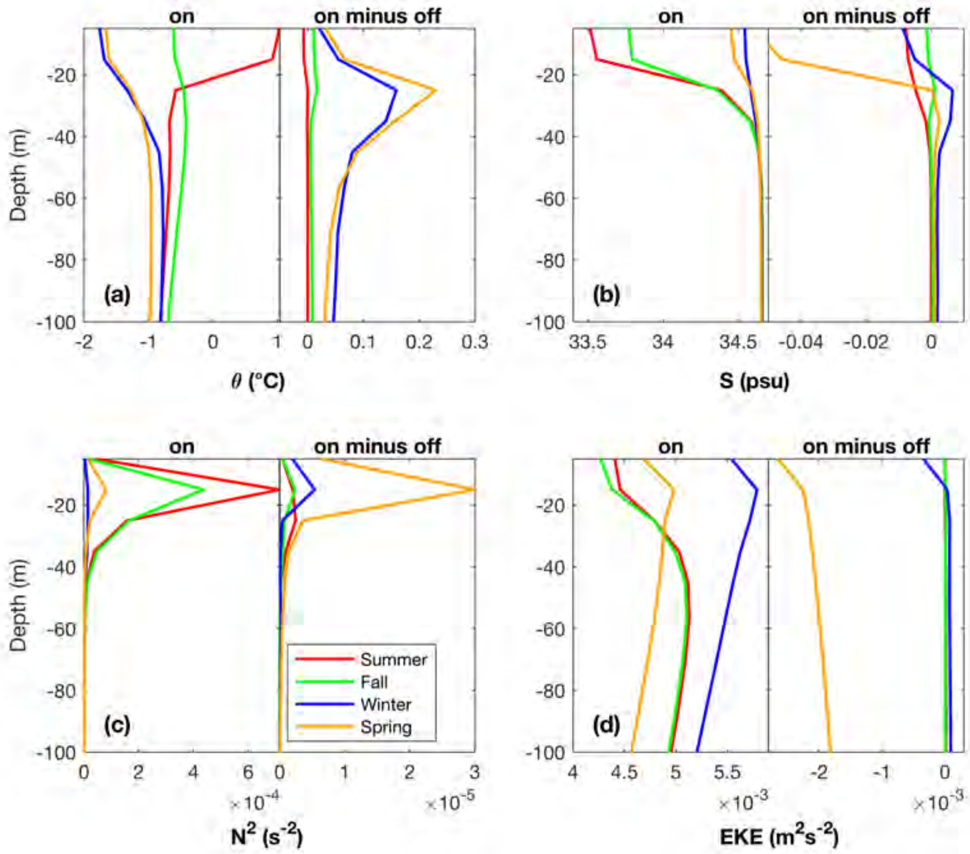

Figure 9. Vertical profiles of (a) θ, (b) S, (c) N^2 and (d) EKE within the seasonal ice zone (y = 400 - 800 km, zonal mean) calculated for the first year of the sensitivity simulation and averaged over seasons: summer in red (JF), fall in green (MAM), winter in blue (JJA), and spring in orange (SON). The left panel of each subplot shows ice stress 'on' and the right panel shows 'on' minus 'off'.

As was shown in Figure 8, EIP tends to warm the ocean near the surface and melt sea-ice during winter and spring in the compact ice zone. Figure 10 reveals that this is immediately followed by anomalous sea-ice formation between November and January (panel (d)), such that the effect of EIP on sea-ice thickness does not build up over the years, but follows a regular seasonal cycle. The recovery and overshoot in sea-ice thickness (panel (c)) is possibly the result of a negative feedback, whereby increased surface stratification following sea-ice melt facilitates surface cooling and sea-ice formation (Martinson (1990), McPhee et al. (1999), Wilson et al. (2019)). EIP brings up warm and salty waters near the surface between May and October (panel (a) and (b)), which causes sea-ice melt during those months and surface freshening between September and December. Panel (d) shows anomalous heat flux out of the ocean between July and the following February, suggesting that the warm SSTs caused by EIP draws anomalous cooling from the atmosphere, which could also contribute to ice recovery

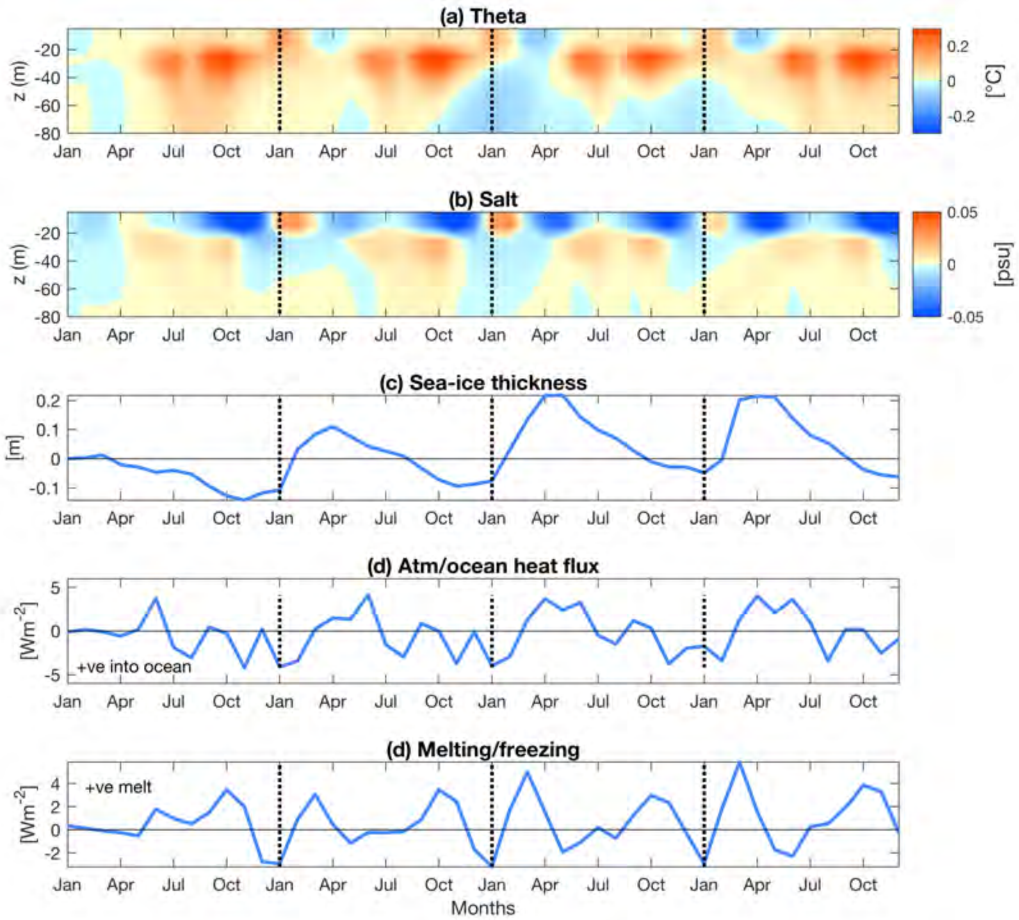

Figure 10. 4-year evolution of the ice stress 'on' minus 'off' simulations for (a) θ, (b) S, (c) area-weighted average sea-ice thickness, (d) net heat flux from the atmosphere to the ocean, and (d) net heat flux to sea-ice. The vertical dotted lines separate each individual year.

6 Discussion and conclusions

In polar oceans, a temperature inversion is typically observed just below the surface in the SIZ, whereby a cold and fresh lens shields sea-ice from underlying warm and salty waters. A number of studies have emphasized the role of vertical heat fluxes originating from these warm waters in controlling the sea-ice thickness, both in the Arctic (Johannessen et al. (1987), Niebauer and Smith Jr. (1989),Carmack et al. (2015)) and the Antarctic (Martinson and Iannuzzi (1989), Worby et al. (2008), Ackley et al. (2015), McKee et al. (2019)). This study presents a process, which we have dubbed the EIP mechanism, by which the frictional coupling between sea-ice and the ocean below can upwell warm waters to the surface and promote melting in the compact ice zone. In regions of densely packed sea-ice, mesoscale eddies feel a surface drag from the relatively stationary ice that generates vertical Ekman velocities and mixes the water column. Numerical simulations in an eddying channel model show that in areas where the sea-ice fraction is higher than 80 %, EIP drives upwelling in anticyclones and downwelling in cyclones, with magnitudes on the order of 1 - 10 m/day. The integrated effect of EIP in our simulations is that of net surface warming, because it raises the temperature beneath the ice in anticyclones without significantly affecting cyclones, whose temperature is already at the freezing point.

In the compact ice zone, EIP reduces sea-ice thickness by 13 cm (10 %) between May and November, due to anomalously large vertical eddy heat fluxes at the surface that peak to 6 Wm^{-2} in September and October. In spring, the anomalous sea-ice melt and upwelling of warm waters increases stratification in the near-surface layers of the ocean, and the mechanical drag from ice reduces EKE throughout the water column. The sea-ice thickness recovers (with an overshoot) the following summer and fall, such that the effect of EIP does not accumulate over the years, but only changes the seasonality of sea-ice. This recovery is likely facilitated by the negative feedback between surface stratification and sea-ice melt (Martinson (1990), McPhee et al. (1999), Wilson et al. (2019)), and the fact that warmer SSTs draw anomalous cooling from the atmosphere between July and March.

The EIP interactions described in this study are analogous to aspects of eddy-wind interactions observed in the open ocean (McGillicuddy et al. (2007), Zhai et al. (2012), Gaube et al. (2015) McGillicuddy (2016), Seo (2017), Song et al. (2020)). At relatively high Rossby numbers, eddies subjected to a large scale wind stress develop a dipole in vertical velocity to balance a vortex tilting tendency (Stern (1965), Niiler (1969)). More-over, the differential enhancement of surface stress on opposite sides of an eddy may drive a monopole in Ekman vertical velocity at the core of the vortex (Dewar & Flierl, 1987). In our simulations, open ocean eddy-wind interactions produce a negligible monopole, and a dipole that only has a modest impact on the vertical velocity w. In the compact ice zone, eddy-wind interactions are also weak, while EIP generates a strong monopole that significantly enhances w. The strength of this monopole reflects the higher effectiveness of EIP in generating an eddy-scale stress curl in regions of pack ice, as compared to large scale winds.

Another distinguishing factor of eddies in the compact ice zone is the thermodynamic modulation of MLDs from sea-ice melting and freezing. In the open ocean, eddies can modulate the MLD through the vertical displacement of isopycnals associated with eddy formation and decay. Our open ocean composites show a deepening of the MLD in anticyclones and a shoaling in cyclones with anomalies on the order of several tens of meters relative to the mean, consistent with previous work (Song et al. (2015) and Hausmann et al. (2017)). In the compact ice zone, however, the MLD shallows in anticyclones due to sea-ice melt ($\sim$ 20 m), and becomes very deep in cyclones ($\sim$ 500 m) due to sea-ice formation and brine rejection. Turning EIP 'off' reduces the MLD shallowing in anticyclones slightly, but does not affect cyclones. We expect that the large differences in MLD between cyclones and anticyclones may have important consequences for tracer transport, nutrient cycling and biological activity in the in the compact ice region (Williams and Follows (1998), McGillicuddy et al. (1998)).

On the large scale, winds typically impart momentum to sea-ice, which may in turn speed up the mean currents. However, the EIP mechanism may extract momentum at smaller scales, when sea-ice is stationary relative to the underling mesoscale eddies. In regions of loose sea-ice, internal ice stresses are too weak to resist the eddy motion, and hence the local difference in ice/ocean velocities is too small for there to be a significant eddy-scale drag. Manucharyan and Thompson (2017) argue that in the Arctic marginal ice zone, in the absence of winds and sea-ice thermodynamics, cyclonic eddies and filaments effectively trap sea-ice due to converging motion at the surface, while anticyclones repel ice due to local divergence. The resulting asymmetry in ice thickness could perhaps be enhanced by the effects of sea-ice melt and freeze discussed in our study, since cyclones are typically cold and anticyclones warm. Finally, the horizontal density gradients observed across eddies in our compact ice zone could trigger submesoscale activity that is currently not resolved in our model. These fine scale processes may generate vertical velocities on the order of 10 - 100 m/day, which may have significant impacts on local dynamics, depending on their coherence and persistence characteristics (Boccaletti et al. (2007), Thomas et al. (2008), Manucharyan and Thompson (2017)).

Appendix A Eddy detection procedure

Eddies are identified based on the following algorithm, based on Chelton et al. (2011) and Song et al. (2015):

1. Find closed contours in sea surface height (SSH) anomaly.

2. Check that the closed contours have more than the minimum number of pixels (75 in the compact ice zone and 500 in the open ocean).

3. Check that there is only one extremum within the closed contours.

4. Check that the amplitude is larger than the minimum threshold (4 cm in the open ocean and 2.5 cm in the compact ice zone).

5. Compute the maximum distance between pixels and check that it doesn't exceed a threshold value (180 px in the open ocean and 100 px in the compact ice zone). This ensures that the eddy shapes are not too different from circles.

The parameter values used in the open ocean are similar to those reported in Song et al. (2015) and the composite results are not highly sensitive to these choices. In the compact ice zone, eddies are typically smaller and weaker than in the open ocean, so parameters were adapted empirically to produce reasonable-looking eddies.

Appendix B Eddy-wind interactions

Eddy-wind interactions modulate both the wind stress and its curl, which can locally enhance vertical velocities through Ekman processes. When the Rossby number is not negligible, there is a non-linear component to the vertical velocity that tends to balance vortex tilting (Stern (1965), Niiler (1969), Wenegrat and Thomas (2017), Song et al. (2020)). Stern (1965) derives the following expression for the total Ekman pumping velocity w_{stern} as follows:

$$
\begin{aligned}
w_{stern} &\approx w_{curl} + w_\zeta \\
&= \frac{\nabla \times \vec{\tau}}{\rho_0 (f+\zeta)} + \frac{\vec{\tau} \times \nabla \zeta}{\rho_0 (f+\zeta)^2} \\
&= \frac{\nabla \times \vec{\tau}}{\rho_0 (f+\zeta)} + \frac{1}{\rho_0 (f+\zeta)^2} \left(\tau_x \frac{\partial \zeta}{\partial y} - \tau_y \frac{\partial \zeta}{\partial x} \right),
\end{aligned}
\tag{B1}
$$

where w_{curl} is the linear Ekman velocity term and w_ζ is the non-linear interaction term. Perpendicular to a uniform wind stress $\vec{\tau}$, the differential enhancement of stress on either side of an eddy can generate a monopole in Ekman suction/pumping at the core of the vortex due to w_{curl}. Additionally, when ζ is not negligible, w_ζ produces a dipole pattern in the direction perpendicular to $\vec{\tau}$.

We consider composites of anticyclones for w_{stern} and the subsurface velocity w_s (Figure B1). In the open ocean, w_{stern} has a dipole pattern mostly aligned with the meridional direction, consistent with w_ζ dominating over w_{curl}, and with winds being predominantly zonal (panels (a) and (b)). w_{stern} only contributes modestly to w_s, whose dipole is stronger and in the zonal direction. In the compact ice zone, when the ice stress is 'on', w_{stern} matches the pattern in w_s better, but does not completely account for it (panels (c) and (d)). When the ice stress is 'off', w_{stern} is negligible, while w_s has a predominantly zonal dipole (panels (e) and (f)). This suggests that the pattern shown in panel (d) is dominated by ice-ocean stresses rather than eddy-wind interactions. We thus conclude that eddy-wind interactions contribute only weakly to the vertical velocity profile of anticyclones, both in the open ocean and in the ice zone. Similar results are obtained for cyclones (not shown).

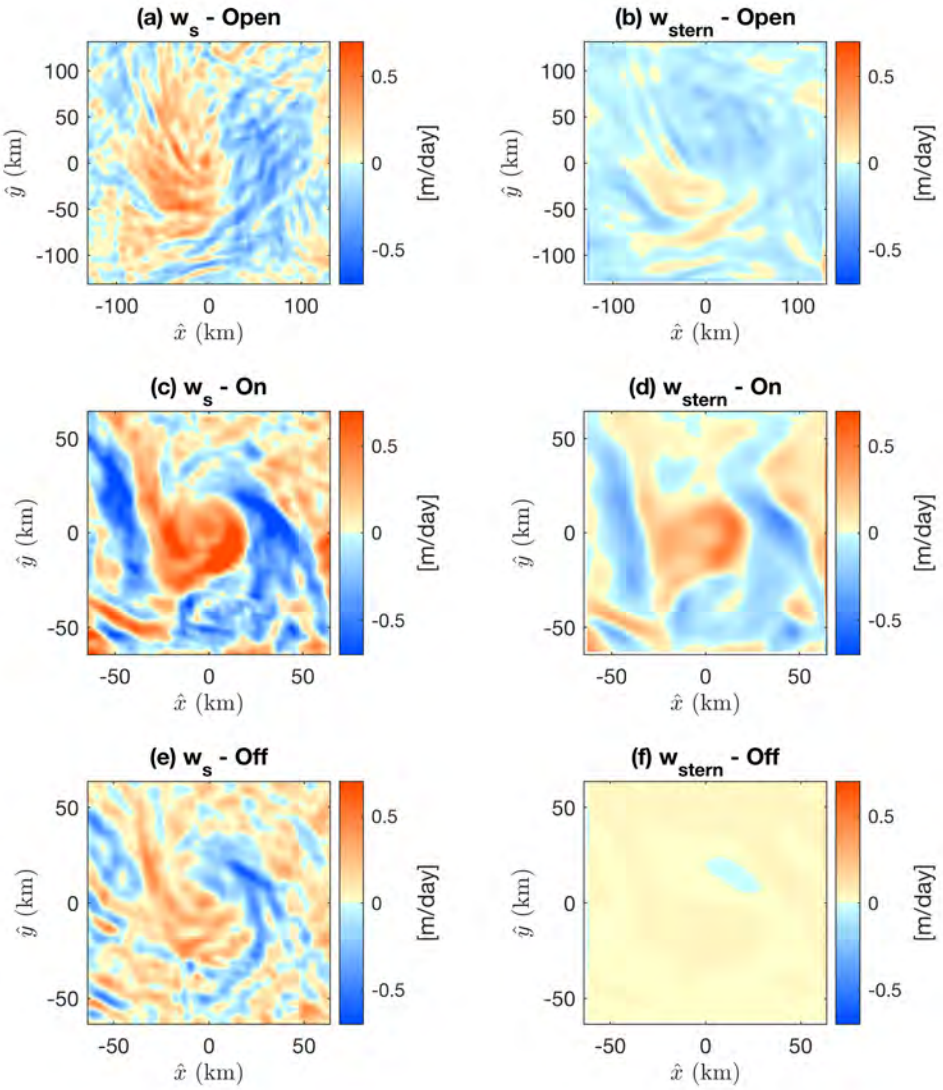

Figure B1. Composite means of anticyclones for w_s (left) and w_{stern} (right). The composites are taken in the open ocean (top), in the compact ice zone with ice stress 'on' (middle) and in the compact ice zone with the ice stress 'off' (bottom).

Acknowledgments

M.G. and J.M. acknowledge support from the NSF Antarctic Program, H.S. acknowledges the support of the National Research Foundation of Korea (NRF) grant funded by the Korean government (MSIT) (NRF-2019R1C1C1003663) and the Yonsei University Research Fund of 2018-22-0053, J-M.C. acknowledges support from the MIT-GISS collaborative agreement, and G.M. acknowledges support from the NSF program on Arctic Research (1603557). We are also grateful for insightful discussions with David Ferreira and Tim Cronin. The MITgcm configuration files used in this study are available at https://doi.org/10.5281/zenodo.3827532.

References

Ackley, S. F., Xie, H., & Tichenor, E. A. (2015). Ocean heat flux under antarctic sea ice in the bellingshausen and amundsen seas: two case studies. *Annals of Glaciology*, *56*(69), 200–210. doi: 10.3189/2015AoG69A890

Adcroft, A., Hill, C., & Marshall, J. (1997). Representation of topography by shaved cells in a height coordinate ocean model. *Monthly Weather Review*, *125*(9), 2293-2315. doi: 10.1175/1520-0493(1997)125⟨2293:ROTBSC⟩2.0.CO;2

Boccaletti, G., Ferrari, R., & Fox-Kemper, B. (2007, September). Mixed Layer Instabilities and Restratification. *Journal of Physical Oceanography*, *37*(9), 2228–2250. Retrieved 2020-02-17, from `http://journals.ametsoc.org/doi/10.1175/JPO3101.1` doi: 10.1175/JPO3101.1

Carmack, E., Polyakov, I., Padman, L., Fer, I., Hunke, E., Hutchings, J., … Winsor, P. (2015, December). Toward Quantifying the Increasing Role of Oceanic Heat in Sea Ice Loss in the New Arctic. *Bulletin of the American Meteorological Society*, *96*(12), 2079–2105. Retrieved 2020-02-17, from `http://journals.ametsoc.org/doi/10.1175/BAMS-D-13-00177.1` doi: 10.1175/BAMS-D-13-00177.1

Chelton, D. B., Schlax, M. G., & Samelson, R. M. (2011). Global observations of nonlinear mesoscale eddies. *Progress in Oceanography*, *91*(2), 167 - 216. Retrieved from `http://www.sciencedirect.com/science/article/pii/S0079661111000036` doi: https://doi.org/10.1016/j.pocean.2011.01.002

Dewar, W. K., & Flierl, G. R. (1987). Some effects of the wind on rings. *Journal of Physical Oceanography*, *17*(10), 1653-1667. doi: 10.1175/1520-0485(1987)017⟨1653:SEOTWO⟩2.0.CO;2

Doddridge, E. W., Marshall, J., Song, H., Campin, J., Kelley, M., & Nazarenko, L. (2019, April). Eddy Compensation Dampens Southern Ocean Sea Surface Temperature Response to Westerly Wind Trends. *Geophysical Research Letters*, *46*(8), 4365–4377. Retrieved 2020-02-17, from `https://onlinelibrary.wiley.com/doi/abs/10.1029/2019GL082758` doi:

10.1029/2019GL082758

Gaspar, P., Grégoris, Y., & Lefevre, J.-M. (1990). A simple eddy kinetic energy model for simulations of the oceanic vertical mixing: Tests at station papa and long-term upper ocean study site. *Journal of Geophysical Research: Oceans*, *95*(C9), 16179-16193. doi: 10.1029/JC095iC09p16179

Gaube, P., Chelton, D. B., Samelson, R. M., Schlax, M. G., & O'Neill, L. W. (2015, January). Satellite Observations of Mesoscale Eddy-Induced Ekman Pumping. *Journal of Physical Oceanography*, *45*(1), 104–132. Retrieved 2020-02-17, from `http://journals.ametsoc.org/doi/10.1175/JPO-D-14-0032.1` doi: 10.1175/JPO-D-14-0032.1

Geiger, C. A., Ackley, S. F., & Hibler III, W. D. (1998). Sea ice drift and deformation processes in the western weddell sea. In *Antarctic sea ice: Physical processes, interactions and variability* (p. 141-160). American Geophysical Union (AGU). Retrieved from `https://agupubs.onlinelibrary.wiley.com/doi/abs/10.1029/AR074p0141` doi: 10.1029/AR074p0141

Hausmann, U., McGillicuddy, D. J., & Marshall, J. (2017, January). Observed mesoscale eddy signatures in Southern Ocean surface mixed-layer depth: SOUTHERN OCEAN EDDY MIXED-LAYER DEPTHS. *Journal of Geophysical Research: Oceans*, *122*(1), 617–635. Retrieved 2020-02-17, from `http://doi.wiley.com/10.1002/2016JC012225` doi: 10.1002/2016JC012225

Hunke, E. C., & Dukowicz, J. K. (1997). An elastic-viscous-plastic model for sea ice dynamics. *Journal of Physical Oceanography*, *27*(9), 1849-1867. doi: 10.1175/1520-0485(1997)027⟨1849:AEVPMF⟩2.0.CO;2

Johannessen, O. M., Johannessen, J. A., Svendsen, E., Shuchman, R. A., Campbell, W. J., & Josberger, E. (1987, April). Ice-Edge Eddies in the Fram Strait Marginal Ice Zone. *Science*, *236*(4800), 427–429. Retrieved 2020-02-17, from `https://www.sciencemag.org/lookup/doi/10.1126/science.236.4800.427` doi: 10.1126/science.236.4800.427

Large, W. G., & Pond, S. (1982). Sensible and latent heat flux measurements over the ocean. *Journal of Physical Oceanography*, *12*(5), 464-482. doi: 10.1175/1520-0485(1982)012⟨0464:SALHFM⟩2.0.CO;2

Large, W. G., & Yeager, S. G. (2009). The global climatology of an interannually varying air–sea flux data set. *Climate Dynamics*, *33*(2), 341–364. doi: 10.1007/s00382-008-0441-3

Locarnini, R. A., Mishonov, A. V., Antonov, J. I., Boyer, T. P., Garcia, H. E., Bara-

nova, O. K., ... Levitus, S. (2013). World ocean atlas 2013. Volume 1, Temperature.
doi: 10.7289/V55X26VD

Losch, M., Menemenlis, D., Campin, J.-M., Heimbach, P., & Hill, C. (2010). On the formulation of sea-ice models. part 1: Effects of different solver implementations and parameterizations. *Ocean Modelling*, *33*(1), 129 - 144. doi: 10.1016/j.ocemod.2009.12.008

Maksym, T. (2019, January). Arctic and Antarctic Sea Ice Change: Contrasts, Commonalities, and Causes. *Annual Review of Marine Science*, *11*(1), 187–213. Retrieved 2020-02-17, from https://www.annualreviews.org/doi/10.1146/annurev-marine-010816-060610 doi: 10.1146/annurev-marine-010816-060610

Manucharyan, G. E., & Thompson, A. F. (2017, December). Submesoscale Sea Ice-Ocean Interactions in Marginal Ice Zones. *Journal of Geophysical Research: Oceans*, *122*(12), 9455–9475. Retrieved 2020-02-17, from https://onlinelibrary.wiley.com/doi/abs/10.1002/2017JC012895 doi: 10.1002/2017JC012895

Marshall, J., Adcroft, A., Hill, C., Perelman, L., & Heisey, C. (1997a). A finite-volume, incompressible Navier Stokes model for studies of the ocean on parallel computers. *Journal of geophysical research: Oceans*. doi: doi.org/10.1029/96JC02775

Marshall, J., Hill, C., Perelman, & Adcroft, A. (1997b). Hydrostatic, quasi-hydrostatic, and non-hydrostatic ocean modelling. *Journal of Geophysical Research: Oceans*. doi: 10.1029/96JC02776

Martinson, D. G. (1990). Evolution of the southern ocean winter mixed layer and sea ice: Open ocean deepwater formation and ventilation. *Journal of Geophysical Research: Oceans*, *95*(C7), 11641-11654. Retrieved from https://agupubs.onlinelibrary.wiley.com/doi/abs/10.1029/JC095iC07p11641 doi: 10.1029/JC095iC07p11641

Martinson, D. G., & Iannuzzi, R. A. (1989). Antarctic ocean-ice interaction: Implications from ocean bulk property distributions in the weddell gyre. , 243-271. doi: 10.1029/AR074p0243

Mauritzen, C., & Häkkinen, S. (1997). Influence of sea ice on the thermohaline circulation in the arctic-north atlantic ocean. *Geophysical Research Letters*, *24*(24), 3257-3260. Retrieved from https://agupubs.onlinelibrary.wiley

.com/doi/abs/10.1029/97GL03192 doi: 10.1029/97GL03192

Mazloff, M. R., Heimbach, P., & Wunsch, C. (2010). An eddy-permitting southern ocean state estimate. *Journal of Physical Oceanography*, *40*(5), 880-899. doi: 10.1175/2009JPO4236.1

McGillicuddy, D. J. (2016, January). Mechanisms of Physical-Biological-Biogeochemical Interaction at the Oceanic Mesoscale. *Annual Review of Marine Science*, *8*(1), 125–159. Retrieved 2020-02-17, from http://www.annualreviews.org/doi/10.1146/annurev-marine-010814-015606 doi: 10.1146/annurev-marine-010814-015606

McGillicuddy, D. J., Anderson, L. A., Bates, N. R., Bibby, T., Buesseler, K. O., Carlson, C. A., … Steinberg, D. K. (2007, May). Eddy/Wind Interactions Stimulate Extraordinary Mid-Ocean Plankton Blooms. *Science*, *316*(5827), 1021–1026. Retrieved 2020-02-17, from https://www.sciencemag.org/lookup/doi/10.1126/science.1136256 doi: 10.1126/science.1136256

McGillicuddy, D. J., Robinson, A. R., Siegel, D. A., Jannasch, H. W., Johnson, R., Dickey, T. D., … Knap, A. H. (1998, July). Influence of mesoscale eddies on new production in the Sargasso Sea. *Nature*, *394*(6690), 263–266. Retrieved 2020-03-04, from http://www.nature.com/articles/28367 doi: 10.1038/28367

McKee, D. C., Martinson, D. G., & Schofield, O. (2019, May). Origin and Attenuation of Mesoscale Structure in Circumpolar Deep Water Intrusions to an Antarctic Shelf. *Journal of Physical Oceanography*, *49*(5), 1293–1318. Retrieved 2020-02-17, from http://journals.ametsoc.org/doi/10.1175/JPO-D-18-0133.1 doi: 10.1175/JPO-D-18-0133.1

McPhee, M. G., Kottmeier, C., & Morison, J. H. (1999). Ocean heat flux in the central weddell sea during winter. *Journal of Physical Oceanography*, *29*(6), 1166-1179. Retrieved from https://doi.org/10.1175/1520-0485(1999)029<1166:OHFITC>2.0.CO;2 doi: 10.1175/1520-0485(1999)029⟨1166:OHFITC⟩2.0.CO;2

Moffat, C., & Meredith, M. (2018). Shelf-ocean exchange and hydrography west of the antarctic peninsula: a review. *Philosophical Transactions of the Royal Society A: Mathematical, Physical and Engineering Sciences*, *376*(2122), 20170164. doi: 10.1098/rsta.2017.0164

Muench, R. D., Morison, J. H., Padman, L., Martinson, D., Schlosser, P., Huber, B., & Hohmann, R. (2001). Maud rise revisited. *Journal of Geophysical Research: Oceans*, *106*(C2), 2423-2440. Retrieved from https://

agupubs.onlinelibrary.wiley.com/doi/abs/10.1029/2000JC000531 doi: 10.1029/2000JC000531

Niebauer, H. J., & Smith Jr., W. O. (1989). A numerical model of mesoscale physical-biological interactions in the fram strait marginal ice zone. *Journal of Geophysical Research: Oceans*, *94*(C11), 16151-16175. Retrieved from https://agupubs.onlinelibrary.wiley.com/doi/abs/10.1029/JC094iC11p16151 doi: 10.1029/JC094iC11p16151

Niiler, P. P. (1969, December). On the Ekman divergence in an oceanic jet. *Journal of Geophysical Research*, *74*(28), 7048–7052. Retrieved 2020-02-17, from http://doi.wiley.com/10.1029/JC074i028p07048 doi: 10.1029/JC074i028p07048

Ohshima, K. I., Nihashi, S., & Iwamoto, K. (2016, May). Global view of sea-ice production in polynyas and its linkage to dense/bottom water formation. *Geoscience Letters*, *3*(1), 13. Retrieved from https://doi.org/10.1186/s40562-016-0045-4 doi: 10.1186/s40562-016-0045-4

Padman, L. (1995). Small-scale physical processes in the arctic ocean. In *Arctic oceanography: Marginal ice zones and continental shelves* (p. 97-129). American Geophysical Union (AGU). Retrieved from https://agupubs.onlinelibrary.wiley.com/doi/abs/10.1029/CE049p0097 doi: 10.1029/CE049p0097

Polyakov, I. V., Pnyushkov, A. V., Alkire, M. B., Ashik, I. M., Baumann, T. M., Carmack, E. C., … Yulin, A. (2017). Greater role for atlantic inflows on sea-ice loss in the eurasian basin of the arctic ocean. *Science*, *356*(6335), 285–291. Retrieved from https://science.sciencemag.org/content/356/6335/285 doi: 10.1126/science.aai8204

Seo, H. (2017). Distinct influence of air–sea interactions mediated by mesoscale sea surface temperature and surface current in the arabian sea. *Journal of Climate*, *30*(20), 8061-8080. doi: 10.1175/JCLI-D-16-0834.1

Sirevaag, A., & Fer, I. (2012). Vertical heat transfer in the arctic ocean: The role of double-diffusive mixing. *Journal of Geophysical Research: Oceans*, *117*(C7). doi: 10.1029/2012JC007910

Song, H., Marshall, J., Gaube, P., & McGillicuddy, D. J. (2015, February). Anomalous chlorofluorocarbon uptake by mesoscale eddies in the Drake Passage region. *Journal of Geophysical Research: Oceans*, *120*(2), 1065–1078. Retrieved 2020-02-17, from http://doi.wiley.com/10.1002/2014JC010292 doi: 10.1002/2014JC010292

Song, H., Marshall, J., McGillicuddy Jr., D. J., & Seo, H. (2020). Impact of current-wind interaction on vertical processes in the southern ocean. *Journal of Geophysical Research: Oceans*, *125*(4), e2020JC016046. doi: 10.1029/2020JC016046

Stern, M. E. (1965). Interaction of a uniform wind stress with a geostrophic vortex. *Deep Sea Research and Oceanographic Abstracts*, *12*(3), 355 - 367. Retrieved from `http://www.sciencedirect.com/science/article/pii/0011747165900070` doi: https://doi.org/10.1016/0011-7471(65)90007-0

Thomas, L. N., Tandon, A., & Mahadevan, A. (2008). Submesoscale processes and dynamics. In M. W. Hecht & H. Hasumi (Eds.), *Geophysical Monograph Series* (Vol. 177, pp. 17–38). Washington, D. C.: American Geophysical Union. Retrieved 2020-02-17, from `http://doi.wiley.com/10.1029/177GM04` doi: 10.1029/177GM04

Timmermans, M.-L., & Marshall, J. (2020). Understanding arctic ocean circulation: A review of ocean dynamics in a changing climate. *Journal of Geophysical Research: Oceans*, *125*(4), e2018JC014378. Retrieved from `https://agupubs.onlinelibrary.wiley.com/doi/abs/10.1029/2018JC014378` (e2018JC014378 10.1029/2018JC014378) doi: 10.1029/2018JC014378

Timmermans, M.-L., Toole, J., Krishfield, R., & Winsor, P. (2008). Ice-tethered profiler observations of the double-diffusive staircase in the canada basin thermocline. *Journal of Geophysical Research: Oceans*, *113*(C1). doi: 10.1029/2008JC004829

Wenegrat, J. O., & Thomas, L. N. (2017, May). Ekman Transport in Balanced Currents with Curvature. *Journal of Physical Oceanography*, *47*(5), 1189–1203. Retrieved 2020-02-17, from `http://journals.ametsoc.org/doi/10.1175/JPO-D-16-0239.1` doi: 10.1175/JPO-D-16-0239.1

Williams, R. G., & Follows, M. J. (1998, July). Eddies make ocean deserts bloom. *Nature*, *394*(6690), 228–229. Retrieved 2020-03-04, from `http://www.nature.com/articles/28285` doi: 10.1038/28285

Wilson, E. A., Riser, S. C., Campbell, E. C., & Wong, A. P. S. (2019, April). Winter Upper-Ocean Stability and Ice–Ocean Feedbacks in the Sea Ice–Covered Southern Ocean. *Journal of Physical Oceanography*, *49*(4), 1099–1117. Retrieved 2020-02-17, from `http://journals.ametsoc.org/doi/10.1175/JPO-D-18-0184.1` doi: 10.1175/JPO-D-18-0184.1

Winton, M. (2000). A reformulated three-layer sea ice model. *Journal of atmospheric and oceanic technology*, *17*(4), 525–531.

Worby, A. P., Geiger, C. A., Paget, M. J., Van Woert, M. L., Ackley, S. F., & DeLiberty, T. L. (2008, May). Thickness distribution of Antarctic sea ice. *Journal of Geophysical Research*, *113*(C5). Retrieved 2020-02-17, from `http://doi.wiley.com/10.1029/2007JC004254` doi: 10.1029/2007JC004254

Zhai, X., Johnson, H. L., Marshall, D. P., & Wunsch, C. (2012, August). On the Wind Power Input to the Ocean General Circulation. *Journal of Physical Oceanography*, *42*(8), 1357–1365. Retrieved 2020-02-17, from `http://journals.ametsoc.org/doi/10.1175/JPO-D-12-09.1` doi: 10.1175/JPO-D-12-09.1

Zweng, M. M., Reagan, J. R., Antonov, J. I., Locarnini, R. A., Mishonov, A. V., Boyer, T. P., . . . Levitus, S. (2013). World ocean atlas 2013. Volume 2, Salinity.
doi: 10.7289/V5251G4D